JOURNAL OF AIRCRAFT
Vol. 46, No. 4, July–August 2009

Aerodynamic Analysis of a Generic Fighter Using Delayed Detached-Eddy Simulation

Tiger L. Jeans*
U.S. Air Force Academy, USAFA, Colorado 80840
David R. McDaniel†
U.S. Air Force, Eglin Air Force Base, Florida 32542
Russell M. Cummings‡
U.S. Air Force Academy, USAFA, Colorado 80840
and
William H. Mason§
Virginia Polytechnic Institute and State University, Blacksburg, Virginia 24061

DOI: 10.2514/1.40955

The modular transonic vortex interaction configuration was developed at the NASA Langley Research Center to investigate the aerodynamic characteristics of a generic fighter incorporating a chined fuselage and delta wing. Previous experiments showed that the fuselage and leading-edge vortex interactions are detrimental to the vehicle's aerodynamic characteristics for angles of attack greater than 23 deg at low angles of sideslip. This is largely due to abrupt asymmetric vortex breakdown, which leads to pronounced pitch-up and significant nonlinearities in lateral stability that could result in roll departure. An improved understanding of the exact origins of this nonlinear behavior would improve future fighter design, and predictive capabilities of such nonlinearities could drastically reduce the cost associated with flight testing new or modified aircraft. The nonlinearities experienced by the modular transonic vortex interaction configuration at a 30 deg angle of attack, Reynolds number of 2.68×10^6, and Mach number of 0.4 are computed using delayed detached-eddy simulation. Computational predictions of rolling moment compare very well with previous wind-tunnel experiments at the same conditions, including the abrupt nonlinear increase in rolling moment as a function of sideslip angle at small sideslip angles. A detailed investigation of the computational fluid dynamic data confirms that this nonlinearity is due to a rapid change in the flowfield structures from symmetric to asymmetric vortex breakdown.

Nomenclature

a = speed of sound
b = wing reference span, 19.20 in.
C_D = stability-axis drag coefficient, $\text{drag}/(q_\infty S)$ |
C_L = stability-axis lift coefficient, $\text{lift}/(q_\infty S)$
C_l = body-axis rolling-moment coefficient, rolling $\text{moment}/(q_\infty Sb)$
C_m = body-axis pitching-moment coefficient, pitching $\text{moment}/(q_\infty S\bar{c})$
C_n = body-axis yawing-moment coefficient, yawing $\text{moment}/(q_\infty Sb)$
C_p = static pressure coefficient, $(p - p_\infty)/q_\infty$
C_{pt} = total pressure coefficient, $(p_t - p_{t\infty})/q_\infty$
C_Y = body-axis side-force coefficient, side $\text{force}/(q_\infty S)$
$\bar{c}$ = wing mean aerodynamic chord, 12.97 in.
l = body length, 32.48 in.
M = Mach number, U/a
p = pressure
p_t = total pressure
q = dynamic pressure, $(\rho U^2)/2$
$Re_{\bar{c}}$ = Reynolds number based on the mean aerodynamic chord, $(\rho U_\infty \bar{c})/\mu$
S = reference wing area, 208.19 in.^{2}
St = Strouhal number
t = time, s
U = velocity magnitude
α = angle of attack, deg
β = angle of sideslip, deg
Δt = time step, s
Δt^* = reduced time step, $(\Delta t U_\infty)/\bar{c}$
ρ = fluid density
μ = dynamic viscosity

Subscript

∞ = freestream conditions

I. Introduction

IN RECENT years, many advanced fighters, such as the F-22 and F-35, have incorporated a chine-shaped forebody designed to minimize observables. Additionally, the chined forebody generally results in stronger forebody vortices, and for certain flight conditions, these vortices interact with the wing leading-edge vortices such that the maneuvering lift capabilities are improved [1]. However, for other flight conditions, these vortex interactions are detrimental to the aerodynamic characteristics of the vehicle. This is especially true when the fighter experiences moderate-to-low angles of sideslip at angles of attack in excess of 25 deg. Under these conditions, abrupt asymmetric vortex breakdown leads to pronounced pitch-up and significant nonlinearities in lateral stability that could result in roll departure [2]. Such asymmetric vortex breakdown has been well

---

Presented as Paper 6228 at the 26th AIAA Applied Aerodynamics Conference, Honolulu, HI, 18–21 August 2008; received 12 September 2008; revision received 9 February 2009; accepted for publication 17 February 2009.

*Visiting Researcher, Department of Aeronautics. Member AIAA.

†Aerospace Engineer, Seek Eagle Office. Member AIAA.

‡Professor, Department of Aeronautics. Associate Fellow AIAA.

§Professor, Department of Aerospace and Ocean Engineering. Associate Fellow AIAA.

documented, however, the exact fluid dynamic mechanisms responsible for this breakdown are unresolved [3].

The vortex interactions of chine fuselage/delta-wing configurations have been extensively investigated experimentally [1–9]. Erickson and Brandon [1] were among the first to investigate the nonlinear aerodynamic and stability characteristics of a chine-shaped forebody and delta-wing configuration. They concluded that at high angles of attack, the chine–wing vortex system was susceptible to severe asymmetries in the core breakdown positions in sideslip. LeMay and Rogers [4] studied pneumatic vortex flow control on a similar configuration and gave two possible reasons for the asymmetric vortex breakdown. First, the chine–wing vortex system interacts such that the chine vortex is pulled down and under the wing vortex and therefore experiences a severe adverse pressure gradient on the wing surface at higher angles of attack. Second, sideslip reduces the effective sweep angle on the windward wing, which increases the strength of the windward vortex system, thereby promoting vortex breakdown, whereas the opposite is true for the leeward wing. Grismer and Nelson [5] studied the aerodynamic effects of a double-delta-wing configuration in sideslip, and they too attributed the asymmetric vortex breakdown to the decrease and increase of the effective sweep angle on the windward and leeward sides, respectively. Rao and Bhat [2,6,7] investigated methods to decouple the forebody and leading-edge vortices. For the purposes of their study, they developed the modular transonic vortex interaction (MTVI) configuration. For their experiments, Mach number varied from 0.4 to 1.2 and Reynolds number ranged from 0.6×10^6 to 2.24×10^6 based on the mean aerodynamic chord. Rao and Bhat found that, in general, leading-edge flaps were very effective at decoupling the forebody and leading-edge vortices, removing the nonlinearities in lateral stability at high angles of attack. They also found that twin vertical tails were effective at accomplishing the same result, whereas a single vertical tail was somewhat effective. Hall [8] studied the impact of the fuselage cross section on the stability of the MTVI body shape without employing leading-edge flaps or vertical tails. He tested a 30 and 100 deg chine cross section in the upright and inverted positions. These experiments were conducted at Mach = 0.4 for Reynolds numbers ranging from 2.61×10^6 to 2.84×10^6. Hall found significant nonlinearities in the rolling moment for all cross sections for $\alpha \geq 23$ deg and -5 deg $< \beta < 5$ deg. He concluded that, in general, the roll stability was much better for the sharper chine angle cross section, and the directional stability was significantly better for the upright configurations.

Significant computational efforts have also been made to fully understand the flow over fighters with chine forebodies [10–21]. Ravi and Mason [10,11] studied the effects of the isolated fuselage on directional stability at high angles of attack and sideslip using both the Euler equations and Reynolds equations employing the Baldwin–Lomax turbulence model. They also developed an analytical model for systematically studying forebody aerodynamics for a family of forebody cross sections. In addition, Agosta-Greenman et al. [12] computationally investigated the effects of tangential slot blowing on an isolated chined forebody using thin-layer Reynolds-averaged Navier–Stokes (RANS) equations. Throughout the mid-1990s, there was a significant joint effort by NASA Langley Research Center, Lockheed Fort Worth Company, Lockheed Aeronautical Systems Company, and The Boeing Company to access the ability of using Euler-based computational fluid dynamic (CFD) codes to predict the aerodynamic characteristics at moderate-to-high alpha for preliminary design. The MTVI configuration was analyzed using the Cartesian-grid SPLITFLOW code [16], multiblock structured-grid TEAM code [17], multiblock overset structured-grid OVERFLOW code [18], and unstructured-grid USM3D code [19]. The general conclusion from this effort was that Euler solutions can provide meaningful guidelines for preliminary design of flight vehicles when dominated by vortical flow. However, for all of these studies, the MTVI configurations included leading-edge flaps, vertical tails, or some combination thereof and therefore did not experience the significant aerodynamic nonlinearities.

Although there has been a significant computational effort to model the flow around the MTVI configuration, to the authors' knowledge, no one has attempted to compute the nonlinear lateral-directional behavior measured by Hall [8]. The goal of this paper is to use delayed detached-eddy simulation [22] (DDES) to computationally predict this nonlinear aerodynamic behavior. Validating state-of-the-art CFD capabilities using extremely nonlinear cases is an essential step to providing a computational tool that can be reliably implemented into the aircraft stability and control analysis. Such a tool would drastically reduce the cost associated with developing future aircraft or modifying existing aircraft. In addition, the CFD predictions provide a high level of detail throughout the entire flowfield that is not available from experiment, and such predictive capabilities are a first step toward offering new insight into the critical fluid dynamic mechanisms responsible for such instabilities. Finally, this work is in support of a larger aircraft stability and control project ongoing at the U.S. Air Force Academy Modeling and Simulation Research Center and the U.S. Air Force Seek Eagle Office. The goal of this project is to develop lower-order predictive models for aerodynamic loads of complete aircraft configurations. The results of this study will be used to help develop and validate these models. The MTVI geometry is an excellent test case due to the nonlinear aerodynamics that occur well within the flight envelope.

The MTVI configuration employed for this study used the 30 deg chine fuselage without leading-edge flaps or vertical tails. A schematic of the overall shape along with the fuselage cross section is shown in Fig. 1. The MTVI body has a span of 29.90 in. and a length of 32.48 in. The wing is composed of a cropped-delta planform with a 60 deg leading-edge sweep and a NACA 65-005 airfoil section modified with double-arc section forward of the maximum thickness and sharp leading edges [6]. Nondimensional forces and moments are calculated relative to the standard body-axis system, with the origin located at the quarter-chord of the mean aerodynamic chord, 20.36 in. from the nose.

II. Computational Methodology

A. Flow Solver

Computations were performed using the commercially available flow solver Cobalt [23], which solves the unsteady, three-dimensional, compressible Navier–Stokes equations. Cobalt is a cell-centered finite-volume-based code applicable to arbitrary cell topologies, including prisms, tetrahedra, and hexahedrals. Second-order accuracy in space is achieved using the exact Riemann solver of Gottlieb and Groth [24] and gradient reconstructions using a least-squares technique. To advance the discretized system, a point-implicit method using analytic first-order inviscid and viscous Jacobians is used. A Newton subiteration method is used in the solution of the system of equations to improve time accuracy of the point-implicit method. The method is second-order-accurate in time. Tomaro et al. [25] converted the code from explicit to implicit, enabling Courant–Friedrichs–Lewy numbers as high as 10^6.

Time-dependent computations were performed using the delayed detached-eddy simulation technique proposed by Spalart et al. [22]. Cobalt has been previously used in conjunction with detached-eddy

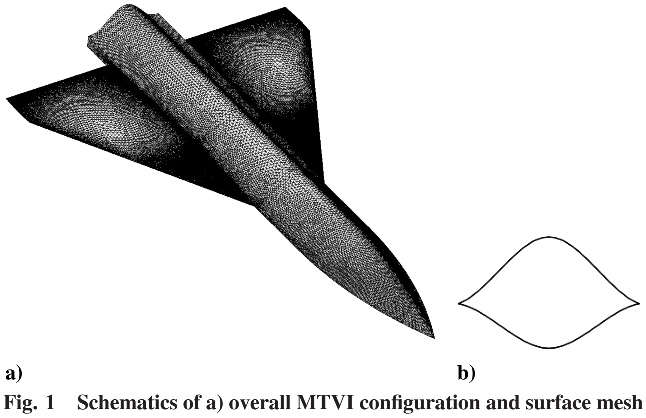

Fig. 1 Schematics of a) overall MTVI configuration and surface mesh and b) forebody cross section with a 30 deg chine.

simulation (DES) to successfully model similar high-angle-of-attack flows [26–28]. DDES is conceptually similar to the original DES technique proposed by Spalart et al. [29], in which the entire boundary layer is treated using a RANS model and highly separated regions are treated using large-eddy simulation (LES). This results in a numerically feasible approach that combines the most favorable elements of each method. Both the original DES model and the DDES model are based on the Spalart–Allmaras (SA) [30] one-equation RANS turbulence model. When the wall destruction term in the SA model is balanced with the production term $\hat{S}$, the eddy viscosity becomes proportional to $\hat{S}d^2$, where d is the distance to the nearest wall. In the Smagorinski LES model, the subgrid-scale turbulent viscosity is described by $\nu_{\mathrm{SGS}} \propto \hat{S}\Delta^2$, where $\Delta = \max(\Delta x, \Delta y, \Delta z)$. Therefore, if d in the wall destruction term of the SA model is replaced with Δ, it will act as the Smagorinski LES model. To exhibit both RANS and LES behavior, d in the SA model is replaced by the DES length scale $\tilde{d}$. The primary difference between DDES and DES is in the definition of the limiter $\tilde{d}$, where the DDES formulation is intended to remove the ambiguous-grid issue emphasized by Menter and Kuntz [31]. Details of the reformulation of $\tilde{d}$ are given by Spalart et al. [22]; however, it is important to note that this new formulation does not represent a minor adjustment within DES. In the original DES formulation, $\tilde{d}$ depended only on the grid, but in the current DDES formulation, $\tilde{d}$ depends on the eddy-viscosity field. Also note that for the current study, the Spalart–Allmaras rotational correction [32] (SARC) turbulence model was implemented. The SARC turbulence model includes modifications to the original SA model to account for the effect of system rotation and/or streamline curvature.

B. Mesh Generation

Generating a quality mesh is essential for an accurate representation of the flow conditions. The meshes used for the current study were created using Solidmesh 3D [33], which is currently being developed at the Mississippi State University. Solidmesh 3D is an advancing-front local-reconnection unstructured-grid generator. An unstructured triangular mesh was generated over the surfaces of the domain and volume elements were then inflated.

A total of four meshes were generated for this study. For each of the meshes, the first node height was chosen using the approach of Cummings et al. [34], such that the average y^+ was below 0.5. This ensures an adequate volume mesh that correctly models the boundary layer. The primary mesh, which will be referred to at the medium-density mesh (MDM), consisted of 10.9 million cells. The medium-density surface mesh is shown in Fig. 1a, and cross-sectional and side views of the mesh elements at $x/l = 0.88$ and $y/l = 0.06$, respectively, are shown in Figs. 2a and 2b. As shown in Fig. 2a, planar mesh controls were implemented above the body such that elements were clustered just above the fuselage and wing to ensure that the forebody and leading-edge vortices were properly convected downstream. To conduct a time-step and grid sensitivity study, two additional meshes were generated with the same topology as the MDM, but the cell spacing was altered such that the total cell counts were approximately 5.5 million cells [referred to as the low-density mesh (LDM)] and 22.6 million cells [referred to as the high-density mesh (HDM)]. A limited number of simulations were completed using a final mesh [referred to as the very fine mesh (VFM)] that consisted of 23.3 million cells. Cross-sectional and side views of the mesh elements are shown in Figs. 2c and 2d. The primary difference between this mesh and the others was that the

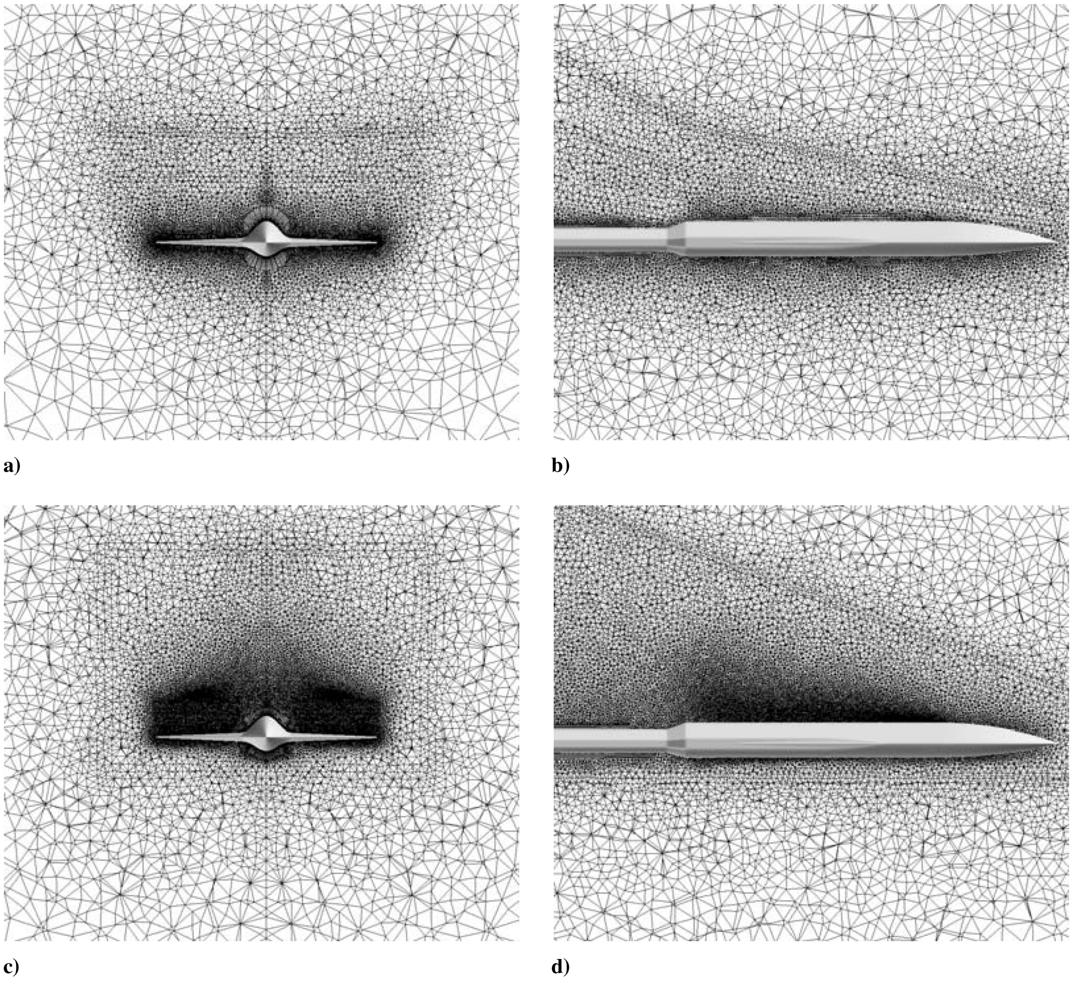

Fig. 2 Two-dimensional mesh schematics: a) cross-sectional view (*x*–*y* plane) of the medium-density mesh at $x/l = 0.89$, b) side view of the medium-density mesh at $y/l = 0.06$, c) cross-sectional view (*x*–*y* plane) of the very fine mesh at $x/l = 0.89$, and d) side view of the very fine mesh at $y/l = 0.06$.

number of cells through the chine and wing vortex cores was significantly increased.

C. Computational Setup

The computational domain was rectangular in shape, with the MTVI geometry centrally located. The minimal distance from the body to each of the outer boundaries was 10*l*. The no-slip adiabatic wall boundary condition was employed for the body surface, and the modified Riemann-invariant condition was implemented as the far-field boundary. Also note that the sting matching used in the previous wind-tunnel experiments [6–8] was incorporated into the geometry. The no-slip adiabatic wall condition without force accounting was implemented on the sting.

Two distinct initial conditions were used for the simulations. The first, referred to as initial condition A, was to initialize the entire domain with the freestream conditions. The second, referred to as initial condition B, was to initialize the entire domain using the flowfield predicted by a previous simulation at similar conditions. For example, the flowfield at $\alpha = 25$ deg and $\beta = 0$ deg was used to initialize the flowfield for the simulation at $\alpha = 30$ deg and $\beta = 0$ deg. It will be shown in the Results and Discussion section that for certain flight conditions, initial conditions A and B result in different solutions.

Time-dependent computations were performed at $Re_{\bar{c}} = 2.68 \times 10^6$ and $M_\infty = 0.40$, which correspond to the experiments of Hall [8] for the 30 deg chine forebody. Simulations were carried out for nominally 7000 to 11,000 time steps, depending on the flowfield conditions, and the first 2000 to 6000 time steps were eliminated to remove transients. This ensured a minimum of 5000 time steps of usable solution. In addition, three Newton subiterations were used to ensure that the flow solution was converged at every time step.

D. Grid Refinement and Time-Step Study

When predicting time-dependent flowfields, it is important to ensure that the mesh density is sufficient such that the solution is spatially converged and the time step is such that the temporal aspects of the flowfield have been sufficiently resolved. Cummings et al. [34] showed that for time-dependent flows, a joint time-step/grid density study is required, because different meshes obtain time independence at different time-step values. They developed a method for ensuring that both temporal and spatial independence have been achieved, which is based on analyzing the frequency content of an

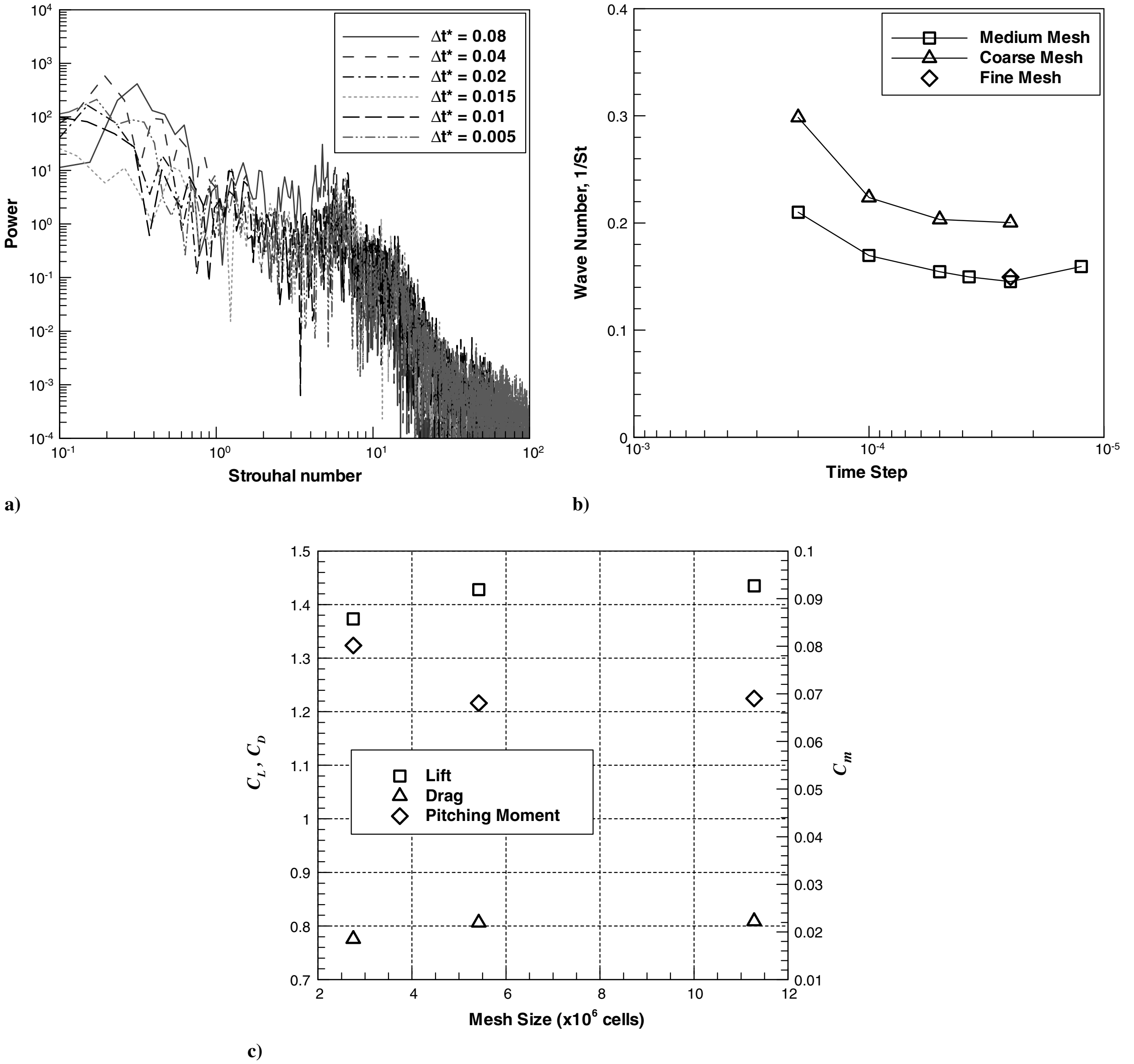

Fig. 3 Pertinent grid refinement and time-step study results: a) variation of the pitching-moment power spectrum density with time step for the medium-density mesh, b) pitching-moment wave-number variation with time step for the low-, medium-, and high-density meshes, and c) variation of time-averaged force and moment predictions with mesh size for $t^* = 0.01$. All results are for $\alpha = 30$ deg, $\beta = 0$ deg, $Re_{\bar{c}} = 2.68 \times 10^6$, and $M_\infty = 0.40$.

appropriate flowfield variable (e.g., integrated forces or moments or pressure at a specific location) using power spectrum density (PSD) analysis. For a given mesh, the time step should be sufficiently small such that dominant flowfield frequencies are time-step-independent.

A grid/time-step study was performed for the geometry at $\alpha = 30$ deg and $\beta = 0$ deg at $Re_{\bar{c}} = 2.68 \times 10^6$ and $M_\infty = 0.40$. Because the study was performed at zero sideslip, symmetry was assumed and only half the domain was modeled. Simulations were completed using the low-, medium-, and high-density meshes for dimensionless time steps ranging from $\Delta t^* = 0.08$ to 0.005, where Δt^* is defined by

$$\Delta t^* = \frac{\Delta t U_\infty}{\bar{c}} \tag{1}$$

For $\Delta t^* = 0.01$, 100 time steps are required for the freestream to travel over the mean aerodynamic chord of the wing. To determine the flowfield frequency content, a PSD analysis of pitching moment was completed for each solution using MATLAB. PSD results for the MDM at various time steps are given in Fig. 3a, which show a dominant flowfield frequency near $St = 7$, where the Strouhal number is defined as

$$St = \frac{f\bar{c}}{U_\infty} \tag{2}$$

Plotted in Fig. 3b are primary frequencies (for $St > 2$) for all of the CFD simulations, which show that $\Delta t^* = 0.01$ is sufficient for the MDM. In addition, a comparison of time-averaged lift, drag, and pitching moment with mesh size is shown in Fig. 3c for $\Delta t^* = 0.01$, which show that integrated forces and moments have converged using the MDM. These results allow one to conclude with a high level of confidence that the solutions are spatially and temporally converged using the MDM in conjunction with $\Delta t^* = 0.01$.

III. Results and Discussion

All of the CFD simulations were performed at the Arctic Region Supercomputing Center on Midnight, a Sun Microsystems cluster composed of 2312 Opteron processors with a 68 TB Lustre file system. The pertinent CFD simulations included in the final data set are listed in Table 1. All of these simulations were performed at $Re_{\bar{c}} = 2.68 \times 10^6$ and $M_\infty = 0.40$ using $\Delta t^* = 0.01$. In addition to the aircraft orientation relative to the freestream, also listed in Table 1 are the corresponding initial condition and mesh for each simulation. Simulations with the same initial condition and mesh are grouped together in the case column, which will be used for identification purposes throughout the remainder of the paper.

Table 1 Pertinent computational fluid dynamics cases included in final data set

Simulation	α, deg	β, deg	Initial condition	Mesh	Case
1	15	0.00	A	MDM	1
2	20	0.00	A	MDM	1
3	25	0.00	A	MDM	1
4	29	0.00	A	MDM	1
5	30	0.00	A	MDM	1
6	30	0.25	A	MDM	1
7	30	0.50	A	MDM	1
8	30	0.75	A	MDM	1
9	30	0.85	A	MDM	1
10	30	1.00	A	MDM	1
11	30	1.15	A	MDM	1
12	30	1.25	A	MDM	1
13	30	1.50	A	MDM	1
14	30	2.00	A	MDM	1
15	30	2.50	A	MDM	1
16	30	3.00	A	MDM	1
17	30	3.50	A	MDM	1
18	30	5.00	A	MDM	1
19	30	0.00	B	MDM	2
20	30	0.25	B	MDM	2
21	30	0.85	B	MDM	2
22	30	1.00	B	MDM	2
23	30	2.00	B	MDM	2
24	40	0.00	B	MDM	2
25	30	0.00	B	MDM	2
26	25	0.00	A	VFM	3
27	30	0.00	A	VFM	3
28	30	0.85	A	VFM	3
29	30	2.00	B	MDM	4
30	30	4.00	B	MDM	4

A. Zero Sideslip

1. *Overall Force and Moment Predictions*

The primary means of validating the DDES predictions is by comparison of overall force and moment coefficients with the experimental data in [8]. A typical CFD time history of total force and moment coefficients is shown in Fig. 4. Once transients were properly removed, the data were averaged using output at every time

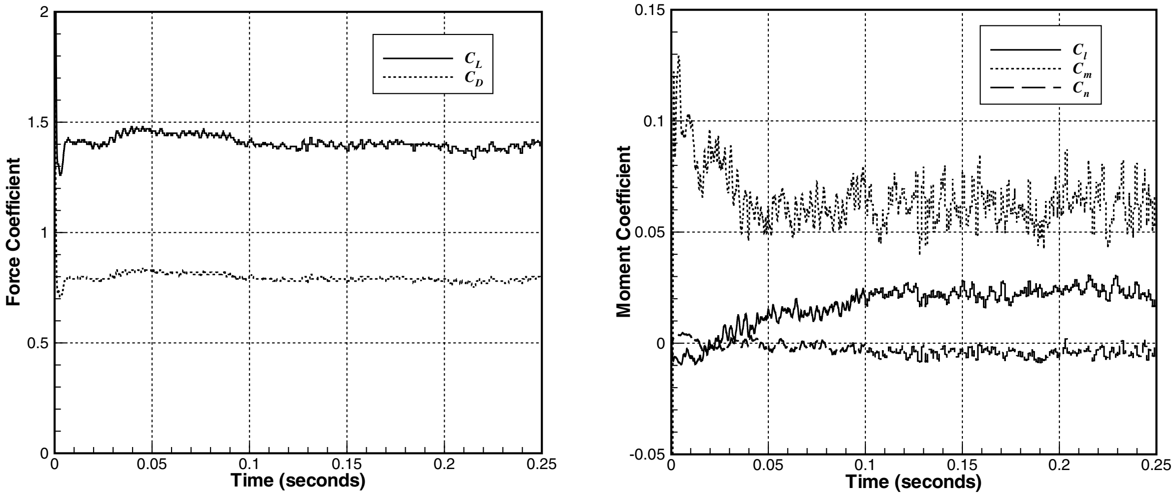

a) b)

Fig. 4 A time history of CFD-predicted a) force coefficients and b) moment coefficients for $\alpha = 30$ deg, $\beta = 1$ deg, $Re_{\bar{c}} = 2.68 \times 10^6$, and $M_\infty = 0.40$.

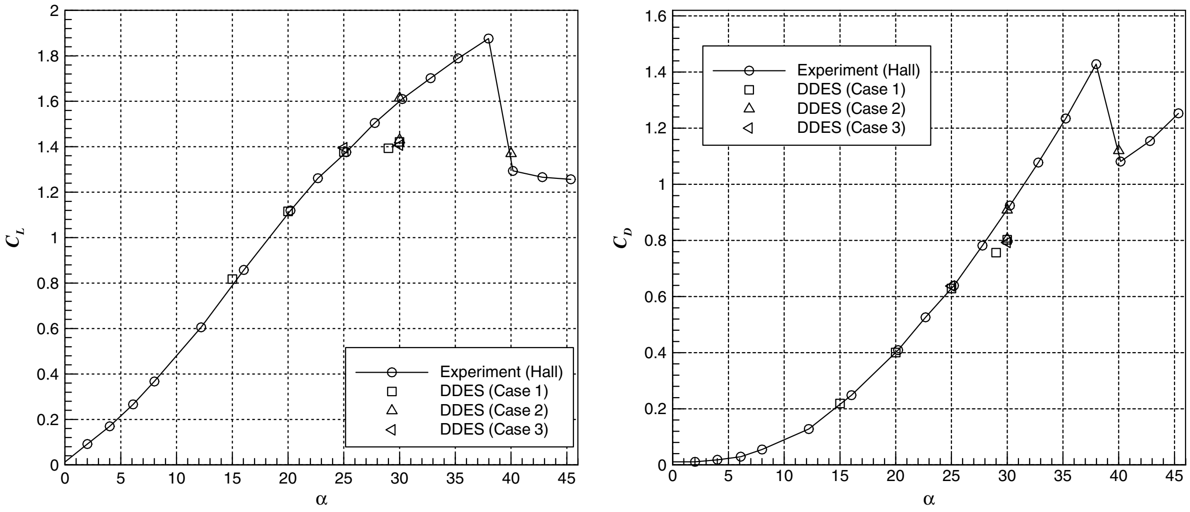

a) Lift

b) Drag

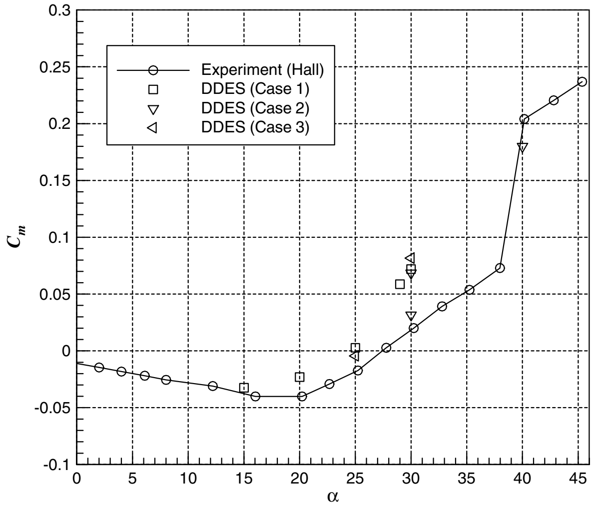

c) Pitching moment

Fig. 5 A comparison of CFD-predicted and experimental lift, drag, and pitching-moment coefficient as a function of α for zero sideslip at $M_\infty = 0.4$ and $Re_{\bar{c}} = 2.68 \times 10^6$.

step to determine mean total force and moment coefficients that could be compared with experimental results.

Time-averaged lift, drag, and pitching-moment coefficients are plotted in Fig. 5 verses angle of incidence for zero sideslip. All of the DDES predictions are in excellent agreement with the experiment for $\alpha \le 25$ deg; however, at incidence angles greater than this, the agreement differs based on the initial conditions used for the DDES simulation. At $\alpha = 30$ deg, initializing the CFD domain to freestream conditions (case 1 and case 3) resulted in solutions that underpredict the experimental lift and drag by approximately 12 and 13%, respectively, whereas initializing the CFD domain using the DDES solution at $\alpha = 25$ deg (case 2) resulted in lift and drag predictions that were again in excellent agreement with experiment. The cause of this discrepancy is discussed further in the next section.

2. *Critical Flow Features*

This section describes some of the critical flow features seen in the $\alpha = 30$ deg and $\beta = 0$ deg results, such that the discrepancies in the lift and drag predictions for cases 1, 2, and 3 are investigated further. All of the data presented in this section (i.e., Figs. 6–8) are time-averaged using results that were output at every 50 time steps.

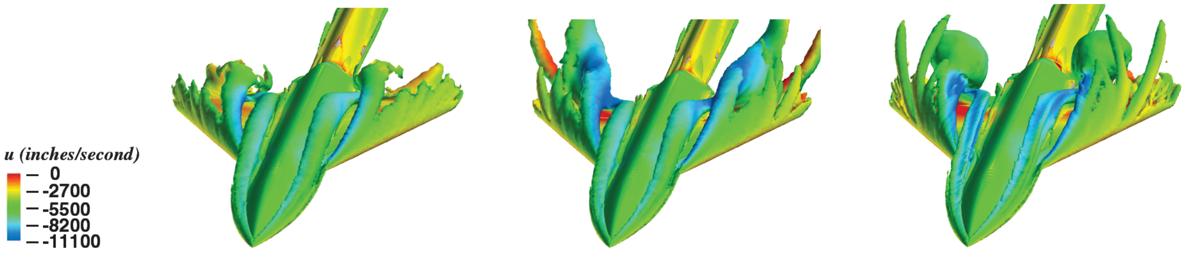

a) Case 1

b) Case 2

c) Case 3

Fig. 6 Isosurfaces of $Q = 1.0 \times 10^7$ s^{-2} for the various DDES simulations at $\alpha = 30$ deg, $\beta = 0$ deg, $Re_{\bar{c}} = 2.68 \times 10^6$, and $M_\infty = 0.40$. The isosurface is colored by axial velocity. Red corresponds to $u = 0$ and blue corresponds to $u = -2u_\infty$.

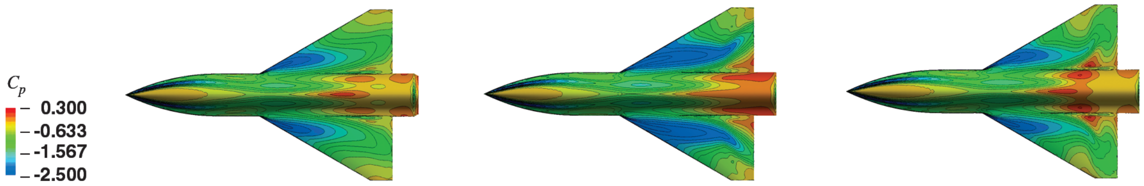

a) Case 1 b) Case 2 c) Case 3

Fig. 7 Top view of surface pressure contours for the various DDES simulations at $\alpha = 30\,\mathrm{deg}$, $\beta = 0\,\mathrm{deg}$, $Re_{\bar{c}} = 2.68 \times 10^6$, and $M_\infty = 0.40$. Red corresponds to $Cp = 0.3$ and blue corresponds to $Cp = -2.5$.

Major vortical structures are highlighted in Fig. 6 using the Q vortex identification criterion [35]. The Q criterion results in a better representation of the main vortical structures than vorticity, because it eliminates the influence of the mean shear in the boundary layer and early shear layers near separation. Plotted in Fig. 6 are isosurfaces of $Q = 1.0 \times 10^7\ \mathrm{s}^{-2}$ for all three simulations completed at zero sideslip and 30 deg incidence. The isosurfaces are colored by axial velocity, with red corresponding to $u = 0$ and blue corresponding to $u = -2u_\infty$. Also note that the left side of each figure is the windward side of the body. The primary fuselage and leading-edge vortices are clearly evident in all of the figures. As shown in Figs. 6a and 6b, the main difference between the cases 1 and 2 results, which both employed the MDM but with different initial conditions, is vortex breakdown. Case 1 predicts symmetric breakdown of both the windward and leeward vortex systems, whereas case 2 predicts no vortex breakdown. A comparison of experimental laser sheet data collected by Hall [8] shows no vortex breakdown at these conditions, which more closely matches case 2 results.

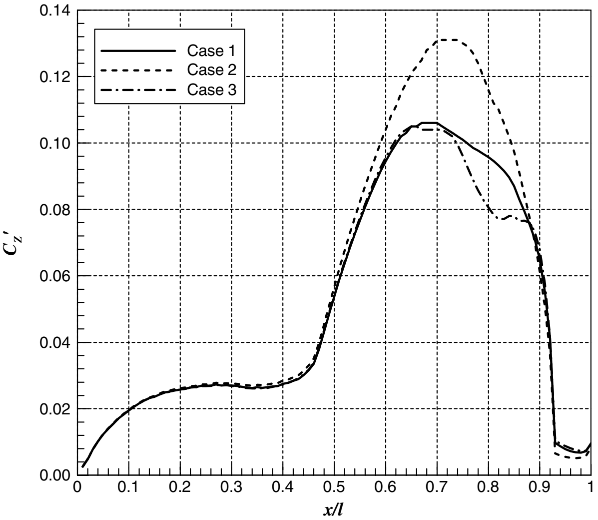

Fig. 8 Axial distribution of normal force for the various simulations at $\alpha = 30\,\mathrm{deg}$, $\beta = 0\,\mathrm{deg}$, $Re_{\bar{c}} = 2.68 \times 10^6$, and $M_\infty = 0.40$.

A detailed investigation was conducted to determine the effect of the different vortex structures predicted by cases 1 and 2 on the total-body-force predictions. Contours of surface pressure C_p for both simulations are plotted in Figs. 7a and 7b. The vortex breakdown predicted in case 1 destroys the low-pressure region on the upper surface of the wing compared with case 2. The extended low-pressure region predicted by case 2 could account for the increase lift and drag predictions presented earlier. This is further reinforced with a comparison of axial normal force distributions C_Z', which are shown in Fig. 8. The vortex breakdown in the case 1 solution causes a significant decrease in the normal force distribution from $x/l = 0.6$ to 0.90.

The differences in the case 1 and case 2 predictions were initially a concern and warranted further investigation. To ensure that the vortex breakdown in case 1 was not a result of artificial vorticity dissipation due to insufficient mesh density, a third simulation that employed the very fine mesh with initial condition A (case 3) was completed. However, as shown in Figs. 6c, 7c, and 8, it also predicted symmetric vortex breakdown, resulting in similar surface pressure and normal force distributions and hence overall force and moment predictions, as with case 1. Two additional simulations were completed at $\alpha = 40$ and 30 deg using the MDM and initial condition A (simulations 24 and 25 in Table 1). Simulation 24 was initialized using the results from simulation 19, which was at $\alpha = 30\,\mathrm{deg}$ and did not predict

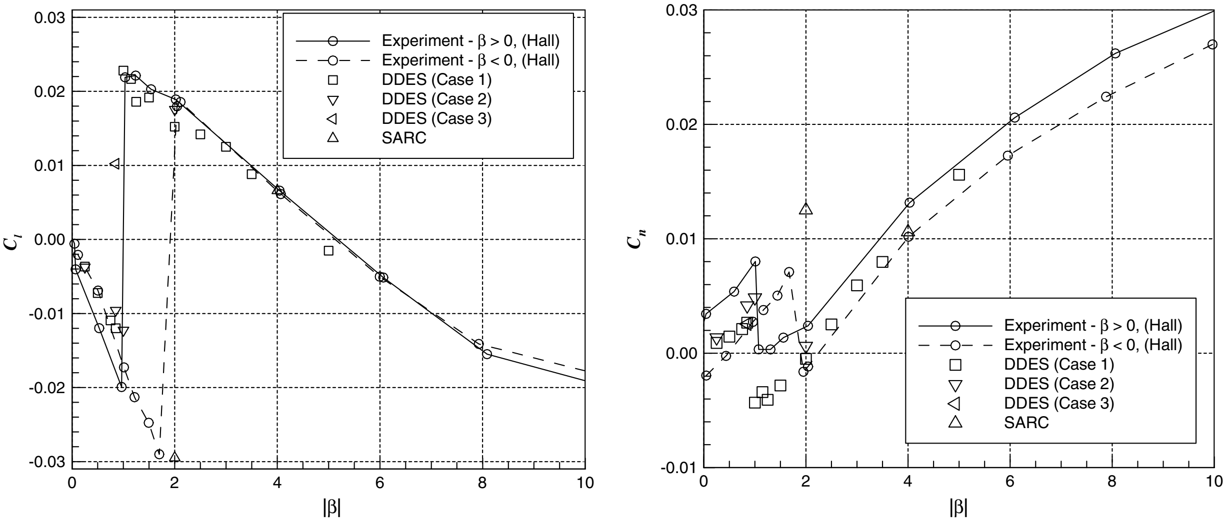

a) b)

Fig. 9 A comparison of CFD-predicted and experimental rolling- and yawing-moment coefficient as a function of β for $\alpha = 30\,\mathrm{deg}$, $M_\infty = 0.4$, and $Re_{\bar{c}} = 2.68 \times 10^6$.

vortex breakdown. As shown in Fig. 5, the body force and moment predictions from this simulation compared well with experimental data, and a detailed investigation of the flowfield indicated symmetric vortex breakdown at this extreme angle of attack. A final simulation (simulation 25) was completed at $\alpha = 30$ deg using the results from $\alpha = 40$ deg to initialize the domain. As shown in Fig. 5, the force and moment predictions did not return to the previous case 2 $\alpha = 30$ deg results, but the predictions compare well with the original cases 1 and 3 $\alpha = 30$ deg predictions, and a detailed investigation of the flowfield indicated symmetric vortex breakdown. These results show a significant hysteresis in the force and moment predictions. Similar hysteresis effects have been previously measured by Grismer and Nelson [36] for a pitching double-delta-wing configuration in sideslip. Their configuration, which exhibits a similar vortex system as the MTVI, resulted in significantly increased lift measurements when pitching upward in incidence, compared with pitching downward in incidence for $\alpha > 25$ deg.

Based on the preceding results, it was concluded that the different CFD solutions predicted by cases 1 and 2 were entirely the result of the different initial conditions employed; however, both are physically correct and are the result of hysteresis. It is important to note that initial condition A is physically similar to placing the model at a fixed angle of attack and starting the wind tunnel, and initial condition B is similar to starting the wind tunnel and pitching the model from low-to-high angles of attack in a quasi-steady manner and then vice versa. The latter is typically how most experiments are

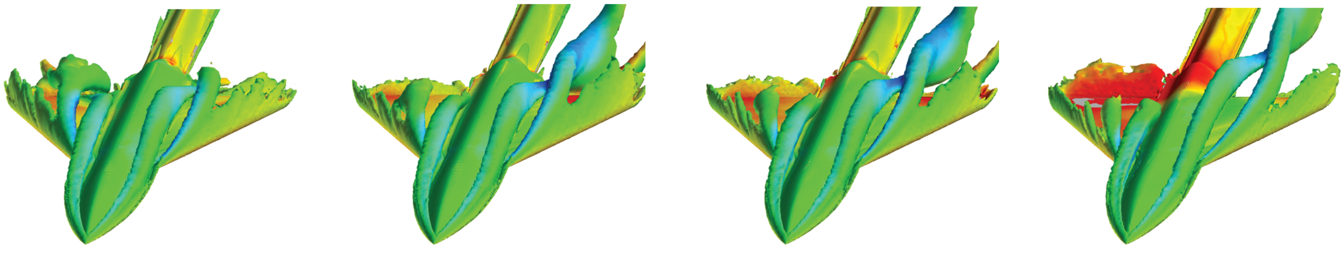
a) $\beta = 0.85$ deg b) $\beta = 1.0$ deg c) $\beta = 2.00$ deg d) $\beta = 5.00$ deg

Fig. 10 Isosurfaces of $Q = 1.0 \times 10^7$ s^{-2} for case 1 simulations at various β for $\alpha = 30$ deg, $M_\infty = 0.4$, and $Re_{\bar{c}} = 2.68 \times 10^6$. The isosurface is colored by axial velocity. Red corresponds to $u = 0$ and blue corresponds to $u = -2u_\infty$. (See Fig. 6 for the contour legend.)

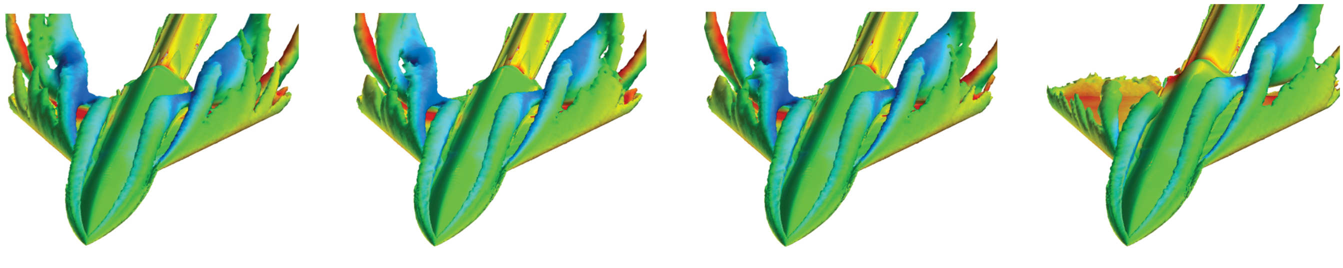
a) $\beta = 0.25$ deg b) $\beta = 0.85$ deg c) $\beta = 1.00$ deg d) $\beta = 2.00$ deg

Fig. 11 Isosurfaces of $Q = 1.0 \times 10^7$ s^{-2} for case 2 simulations at various β for $\alpha = 30$ deg, $M_\infty = 0.4$, and $Re_{\bar{c}} = 2.68 \times 10^6$. The isosurface is colored by axial velocity. Red corresponds to $u = 0$ and blue corresponds to $u = -2u_\infty$. (See Fig. 6 for the contour legend.)

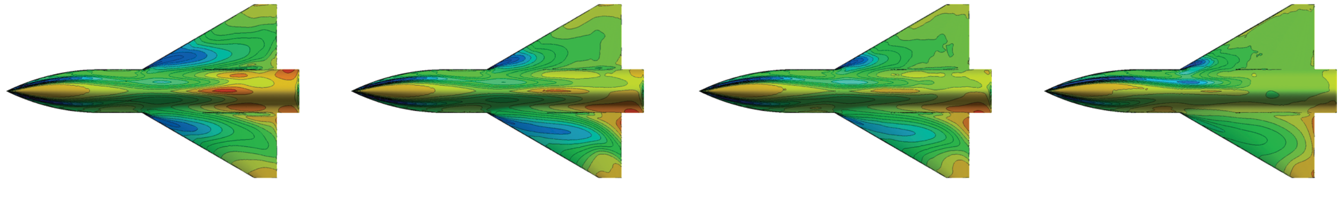
a) $\beta = 0.85$ deg b) $\beta = 1.0$ deg c) $\beta = 2.00$ deg d) $\beta = 5.00$ deg

Fig. 12 Top view of surface pressure contours for case 1 simulations at various β for $\alpha = 30$ deg, $M_\infty = 0.4$, and $Re_{\bar{c}} = 2.68 \times 10^6$. Red corresponds to $Cp = 0.3$ and blue corresponds to $Cp = -2.5$. (See Fig. 7 for the contour legend.)

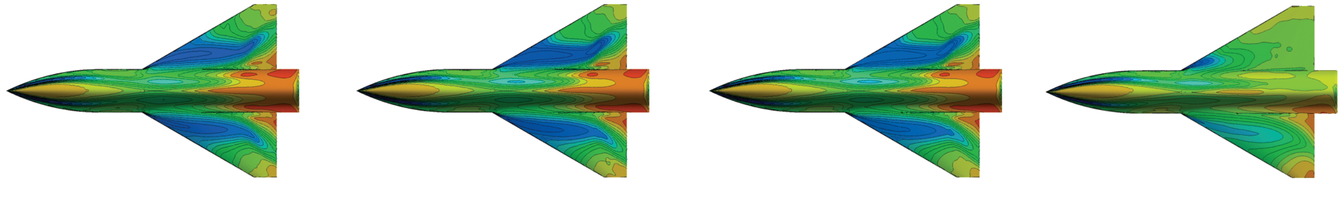
a) $\beta = 0.25$ deg b) $\beta = 0.85$ deg c) $\beta = 1.00$ deg d) $\beta = 2.00$ deg

Fig. 13 Top view of surface pressure contours for case 2 simulations at various β for $\alpha = 30$ deg, $M_\infty = 0.4$, and $Re_{\bar{c}} = 2.68 \times 10^6$. Red corresponds to $Cp = 0.3$ and blue corresponds to $Cp = -2.5$. (See Fig. 7 for the contour legend.)

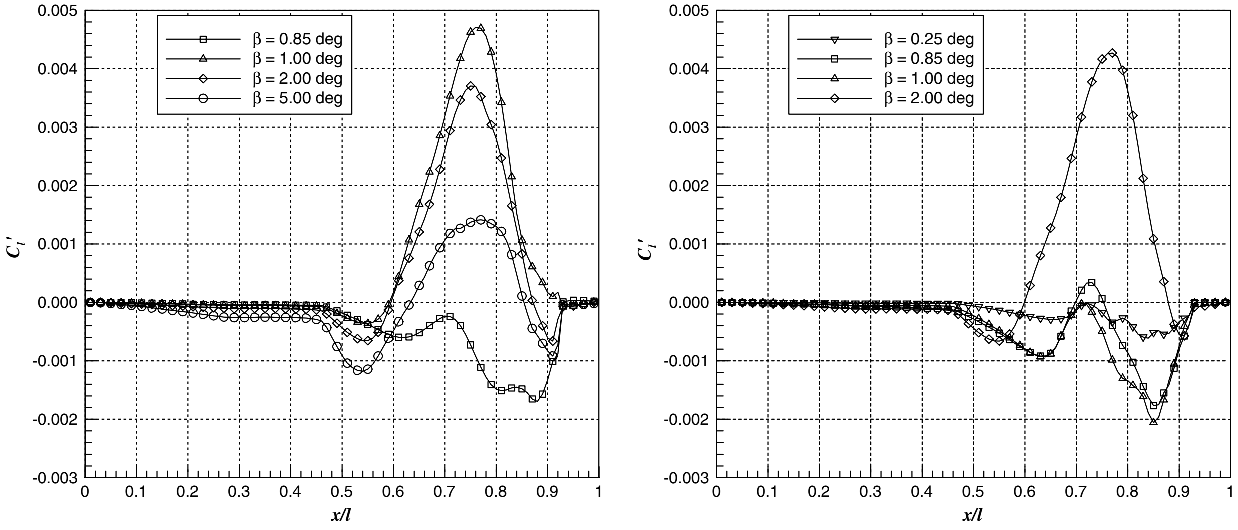

a) Case 1

b) Case 2

Fig. 14 Axial distributions of rolling moment, C_l', at various β for $\alpha = 30\,\text{deg}$, $M_\infty = 0.4$, and $Re_{\bar{c}} = 2.68 \times 10^6$.

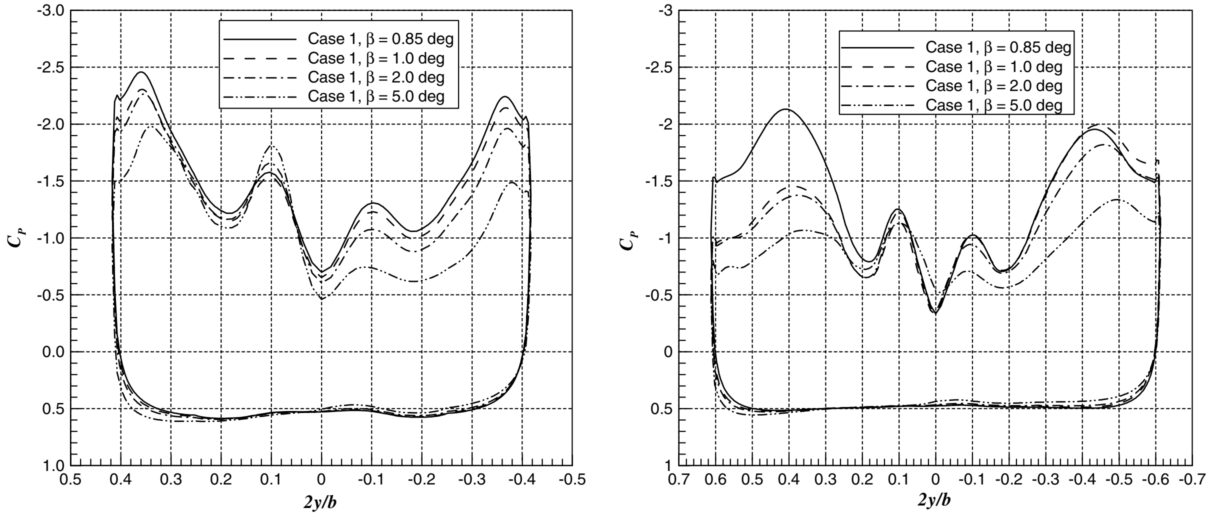

a) *x/l* = 0.55

b) *x/l* = 0.65

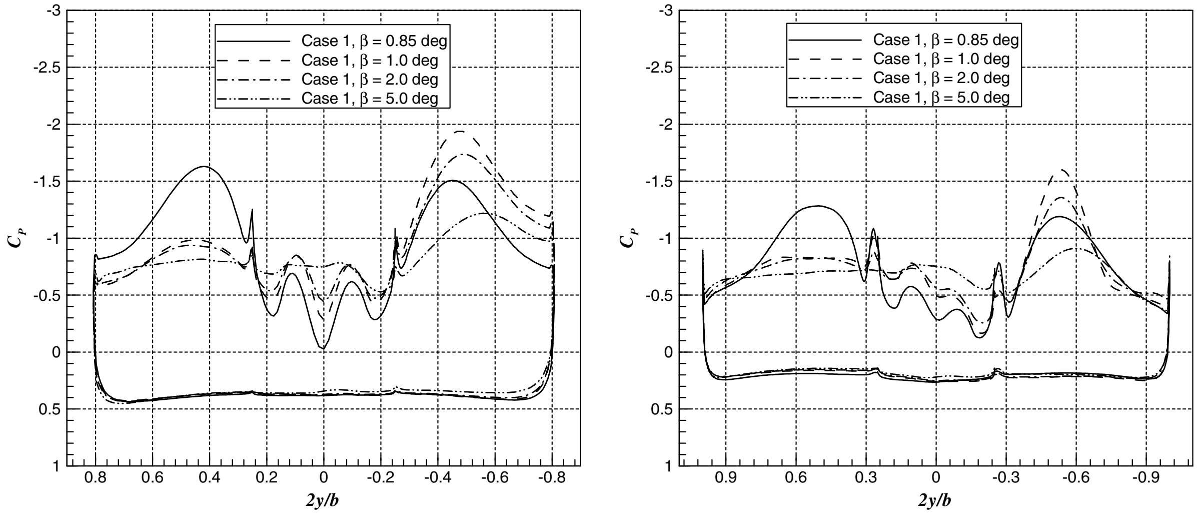

c) *x/l* = 0.75

d) *x/l* = 0.85

Fig. 15 Pressure distributions at constant axial locations for case 1 simulations at various β for $\alpha = 30\,\text{deg}$, $M_\infty = 0.4$, and $Re_{\bar{c}} = 2.68 \times 10^6$.

conducted and is likely how the experimental data were collected by Hall [8]. Thus, when trying to validate CFD results to experimental data in the nonlinear high-angle-of-attack flight regime, it is important to know the manner in which the experimental data were taken and to initialize the CFD domain appropriately.

B. Sideslip at a 30-Degree Angle of Attack

1. *Overall Moment Predictions*

A comparison of DDES predicted and experimentally measured rolling- and yawing-moment coefficients as a function of sideslip are given in Fig. 9. As in Sec. III.A.1, transients were properly removed and the remaining data were averaged using output at every time step. To highlight the hysteresis in the experimental data, both positive and negative sideslips are plotted on the same axis. Computational results are shown for both cases 1 and 2 simulations. Note that employing initial conditions A and B has less of an effect on the rolling- and yawing-moment predictions than lift, drag, and pitching moment. As seen in Fig. 9a, the DDES rolling-moment predictions for both cases 1 and 2 simulations compare very well with the experiment, accurately predicting both the location and magnitude of the nonlinearity at approximately $\beta = 1$ deg. The DDES yawing-moment predictions in Fig. 9b are qualitatively similar to the experimental results. DDES correctly predicts both the nonlinearity at $\beta = 1$ deg and the magnitude of the upward shift in C_n due to this nonlinearity. However, there is a general downward shift in all of the DDES yawing-moment predictions between 0 deg $< \beta < 2$ deg. The exact cause of this discrepancy is still under investigation.

2. *Critical Flow Features*

This section presents the critical flow features in all the simulations with sideslip, such that the causes of the rolling-moment nonlinearity are highlighted. As in Sec. III.A.2, all of the data presented in this section (Figs. 10–16) are timed-averaged using results that were output at every 50 time steps.

The major vortical structures are again highlighted using the Q vortex identification criterion. Isosurfaces of Q contoured by axial velocity are plotted in Figs. 10 and 11 for cases 1 and 2 simulations at various sideslip angles. In general, the topology of the vortical structures for $\beta < 1$ deg are similar, and there is a distinct change in the vortical structures for $\beta > 1$ deg. For all the case 1 simulations at $\beta < 1$ deg, the fuselage and leading-edge vortical structures over both the windward and leeward wings start to intertwine before bursting near the trailing edge. For all the case 2 simulations at $\beta < 1$ deg, the fuselage and leading-edge vortical structures over both the windward and leeward wings intertwine. Again, the primary difference between the cases 1 and 2 results is the vortex breakdown seen in case 1. For both cases 1 and 2 simulations, there is a distinct asymmetry in the vortical structures between the windward and leeward sides for $\beta > 1$ deg. Note from Figs. 10c and 11d, which are both at $\beta = 2$ deg, that case 1 and case 2 predict nearly identical

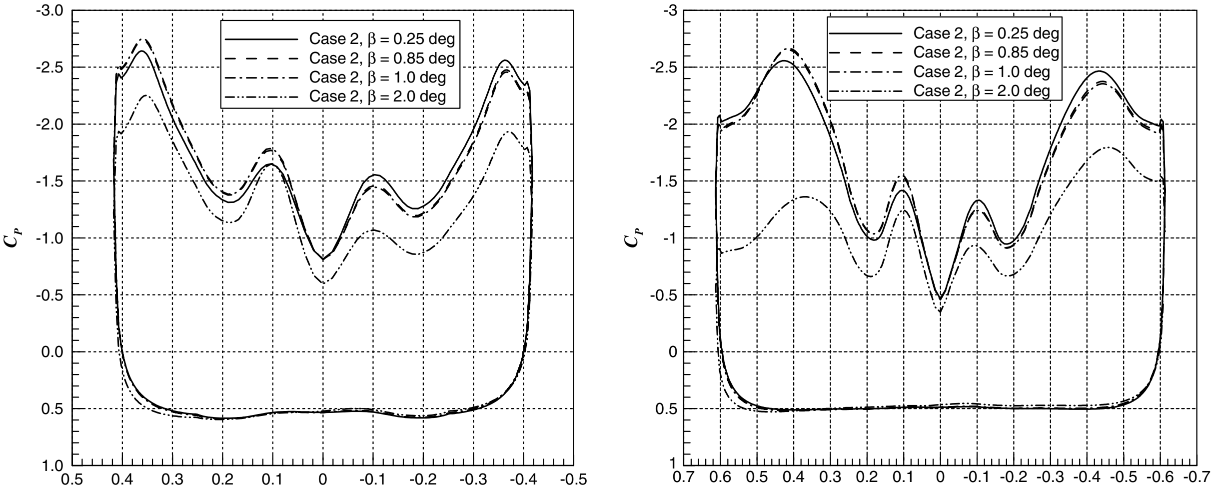

a) *x/l* = 0.55 **b) *x/l* = 0.65**

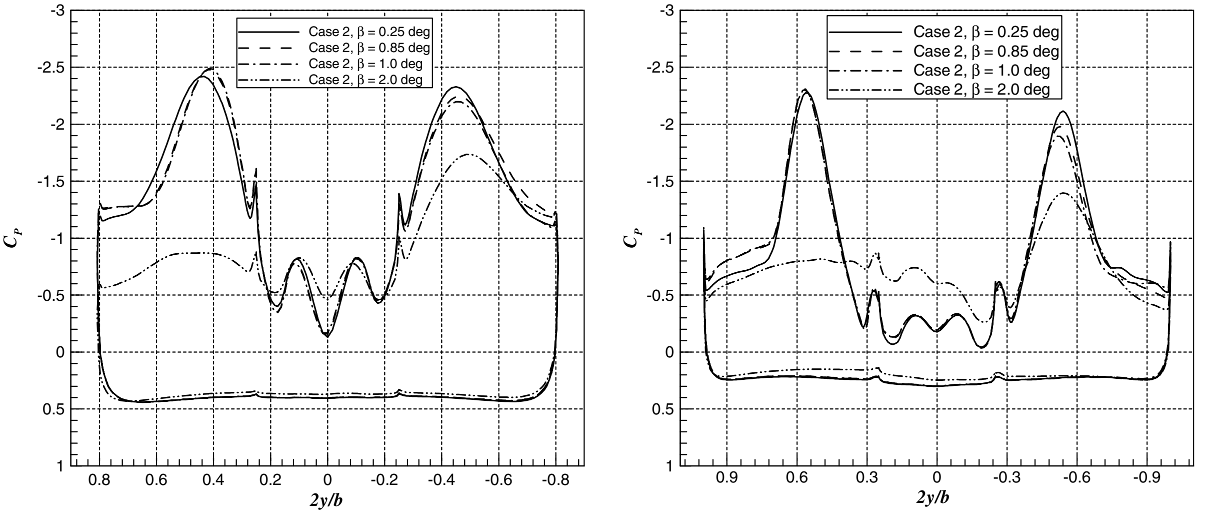

c) *x/l* = 0.75 **d) *x/l* = 0.85**

Fig. 16 Pressure distributions at constant axial locations for case 2 simulations at various β for $\alpha = 30$ deg, $M_\infty = 0.4$, and $Re_{\bar{c}} = 2.68 \times 10^6$.

flowfields. The vortical structures over the windward wing burst, whereas the vortical structures over the leeward wing interact and remain as coherent structures for the full body length. It is these asymmetrical vortex structures that induce the nonlinearities in both rolling and yawing moments.

To investigate the influence of the vortical structures on the surface pressure, contours of surface pressure C_p are plotted in Figs. 12 and 13 for cases 1 and 2, respectively, at the corresponding sideslip angles in Figs. 10 and 11. For all simulations at $\beta < 1$ deg, there is a low-pressure region evident on both the windward and leeward wings due to the leading-edge and chine vortices. By comparison of Fig. 12a with Figs. 13a–13c, one can see that for the case 2 results, these low-pressure regions are extended much further downstream. This is partially due to the increased interactions of the leading-edge and chine vortices, which pull the chine vortex downward and outboard, thereby causing a greater influence on the surface pressure. In addition, from Figs. 7, 12, and 13, one can see that at $\beta = 0$ deg, these low-pressure regions are symmetric, but as sideslip increases to $\beta = 0.85$ deg, the leeward low-pressure region is diminished, which would account for the negative rolling moment at this sideslip. For $\beta > 1$ deg, the forward movement of the windward vortex breakdown significantly reduces the size of the windward low-pressure region in both the cases 1 and 2 results. In addition, the lack of vortex breakdown on the lee side increases the size of the low-pressure region for the case 1 results, whereas the case 2 results remains relatively unchanged. Conceptually, this rapid change to an asymmetric surface pressure distribution could cause the abrupt increase in rolling moment shown in Fig. 9. As sideslip continues to increase beyond $\beta = 1$ deg, the leeward low-pressure region continually diminishes. Closer investigation of Fig. 10d indicates that this is because the leeward vortical structures are displaced further from the body as sideslip is increased and therefore have less effect on the surface pressure distribution. This would correspond to a decreasing rolling moment with increasing sideslip in this region, which is in agreement with Fig. 9.

To further investigate the source of the nonlinear rolling-moment behavior, plotted in Fig. 14 are axial distributions of sectional rolling moment C_l', where the integrated distribution is equal to the total rolling-moment coefficients. Plotted in Fig. 14a are distributions based on case 1 results, and in Fig. 14b are distributions based on case 2 results. All of the distributions exhibit nearly a zero contribution to the rolling moment along the chined forebody. One exception to this is the case 1 simulation at $\beta = 5.0$ deg, which experiences a small negative rolling moment along much of the nose. The primary differences in the distributions occur along the wing between $x/l = 0.5$ and 0.92. For $\beta < 1$ deg, there is generally a negative contribution to the rolling moment along the wing, although some distributions do experience a small positive contribution between $x/l = 0.70$ and 0.75. For $\beta > 1$ deg, there is generally a large positive contribution to the rolling moment along the wing. The distributions increase rapidly and nonlinearly up to a maximum value at approximately $x/l = 0.75$, at which point they decline over the remainder of the wing. As sideslip is increased beyond $\beta = 1$ deg, the maximum value of C_l' decreases from 0.0045 at $\beta = 1$ deg to 0.00125 at $\beta = 5$ deg. Also note that the distributions are nearly symmetric about $x/l = 0.75$.

The sectional rolling-moment distributions are complemented with axial distributions of pressure in Figs. 15 and 16. Distributions are plotted for $x/l = 0.55$, 0.65, 0.75, and 0.85 for each distribution shown in Fig. 14. At $x/l = 0.55$, all of the pressure distributions are asymmetric, such that a local negative rolling moment is induced. This is due to increased suctions on the windward side by both the wing leading-edge and chine vortices. At $x/l = 0.65$, 0.75, and 0.85, there are significant differences in the distributions between all the simulations in which $\beta < 1$ deg and $\beta > 1$ deg. For the simulations with $\beta < 1$ deg, the distributions are similar to those seen at $x/l = 0.55$, whereby the suction peaks induced by the windward

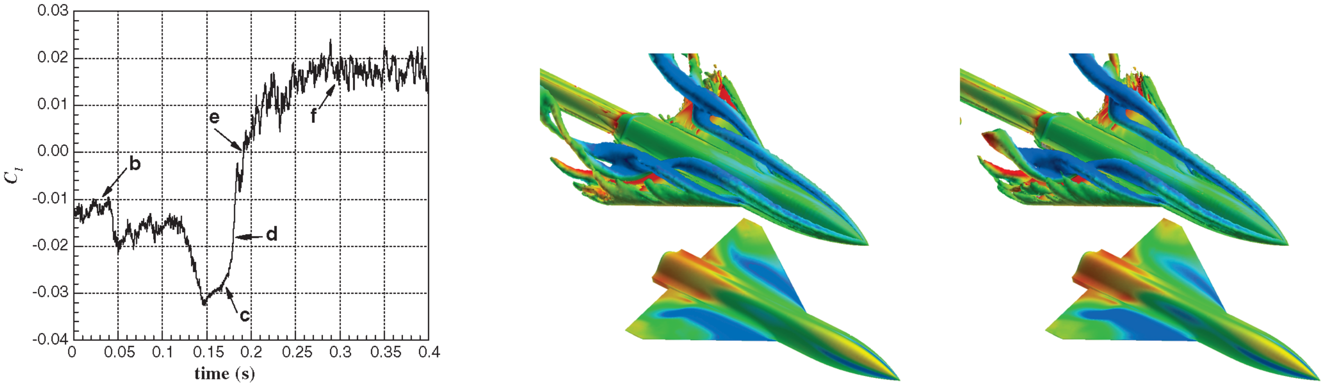

a) Rolling-moment coefficient **b) Time = 0.03 seconds** **c) Time = 0.17 seconds**

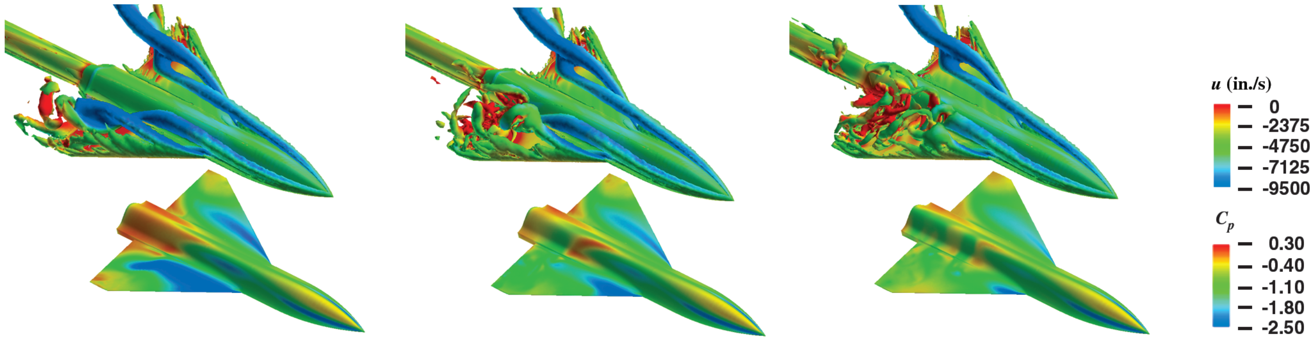

d) Time = 0.18 seconds **e) Time = 0.19 seconds** **f) Time = 0.3 seconds**

Fig. 17 Vortex breakdown dynamics highlighting a) time history of the rolling-moment response for simulation 23 and b–f) isosurfaces of $Q = 1.5 \times 10^7\ \mathrm{s}^{-2}$ contoured by axial velocity and surface pressure coefficients at various times for simulation 23. All results are for $\alpha = 30$ deg, $\beta = 2$ deg, $Re_{\bar{c}} = 2.68 \times 10^6$, and $M_\infty = 0.40$.

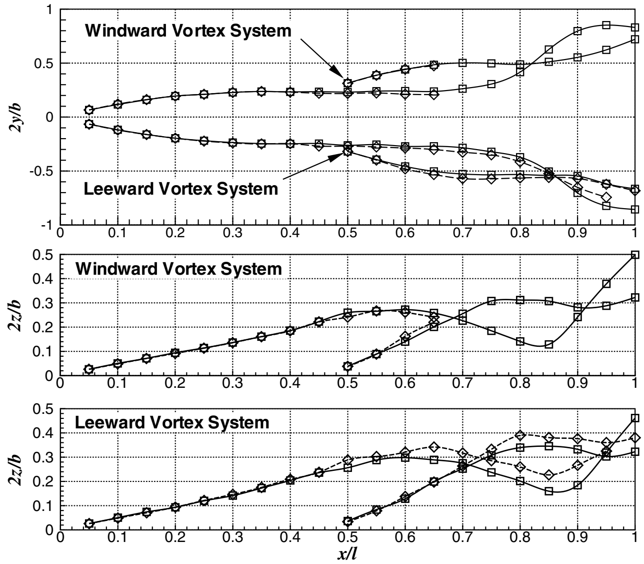

Fig. 18 Vortex trajectories based on minimum total pressure for case 2 simulations at $\beta = 1\,\mathrm{deg}$ and 2.00 deg for $\alpha = 30\,\mathrm{deg}$, $M_\infty = 0.4$, and $Re_{\bar{c}} = 2.68 \times 10^6$. Squares represent $\beta = 1\,\mathrm{deg}$ and diamonds represent $\beta = 2\,\mathrm{deg}$.

vortices induce a small negative local rolling moment. Note that for the case 2 simulations ($\beta = 0.25$, 0.85, and 1.0 deg), the primary suction peaks are significantly larger over the entire wing, compared with the case 1 simulation ($\beta = 0.85\,\mathrm{deg}$); however, the loss of primary suction in the case 1 simulation occurs on both the windward and leeward sides, such that the local rolling-moment predictions remain relatively unchanged. For the simulations with $\beta > 1\,\mathrm{deg}$, there is a significant loss of primary windward suction at $x/l = 0.65$, 0.75, and 0.85 due to the breakdown of the windward vortex system. This results in an asymmetric vortex distribution that induces a strong local positive rolling moment. Also note that this asymmetry is decreased as sideslip increases to $\beta = 5\,\mathrm{deg}$, primarily because the primary suction on the leeward side continually diminishes with increasing sideslip.

3. *Comparison with Reynolds-Averaged Navier–Stokes Simulations*

For comparison, two RANS simulations were completed using the SARC turbulence model. These are simulations 29 and 30 in Table 1 and are identified as case 4. The first simulation was completed at $\alpha = 30\,\mathrm{deg}$ and $\beta = 2\,\mathrm{deg}$, and simulation 22 results were used to initialize the domain. The second simulation was completed at $\alpha =$ 30 deg and $\beta = 4\,\mathrm{deg}$, and the previous RANS simulation results were used to initialize the domain. Steady-state rolling- and yawing-moment predictions are shown in Fig. 9. Overall, the RANS simulations predict the nonlinear behavior reasonably well. A key difference from the DDES simulations is that the nonlinearity is delayed beyond $\beta = 2\,\mathrm{deg}$, resulting in significantly different moment predictions at $\beta = 2\,\mathrm{deg}$. However, at $\beta = 4\,\mathrm{deg}$, the RANS simulation does predict the breakdown of the windward vortex system, and the moment predictions compare well with both the experimental and DDES data. A significant advantage of the DDES simulations over the RANS simulations is that they are able to capture the time-accurate and unsteady nature of the vortex breakdown, as highlighted in Sec. III.C.

C. Vortex Breakdown Dynamics

One major advantage of CFD over wind-tunnel experimentation is that once you have a verified and validated solution, you then have complete access to both the temporal and spatial flowfields, which can be analyzed in detail. For the current study, simulation 23 is especially interesting because it captures the time-accurate vortex breakdown when the sideslip angle is instantaneously increased from $\beta = 1$ to 2 deg. Plotted in Fig. 17a is the time history of the rolling-moment response. Plotted in Figs. 17b–17f are isosurfaces of $Q = 1.5 \times 10^7\ \mathrm{s}^{-2}$ contoured by axial velocity and surface pressure coefficient at $t = 0.03$, 0.17, 0.18, 0.19, and 0.30 s. From $t = 0.03$ to 0.17 s, there is a significant negative increase in rolling moment from $C_l \approx -0.012$ to ≈ -0.028. Inspection of Figs. 17b and 17c indicates that this increase is due to an increased suction on the upper surface of the windward wing and a decrease in suction on the upper surface of the leeward wing. This change in surface pressure distribution is due to an increased interaction of the windward vortex system and a small upward and outboard movement of the leeward vortex system. From $t = 0.17$ to 0.30 s, there is a rapid increase in the rolling moment to its steady value of $C_l \approx 0.018$. Figures 17d–17f capture the dynamic vortex breakdown of the windward vortex system during this time period. The breakdown is initiated at the delta-wing trailing edge and then moves abruptly forward to a final stable position near the leading edge. This change in vortex structure significantly reduces the strong suction on the upper windward wing surface.

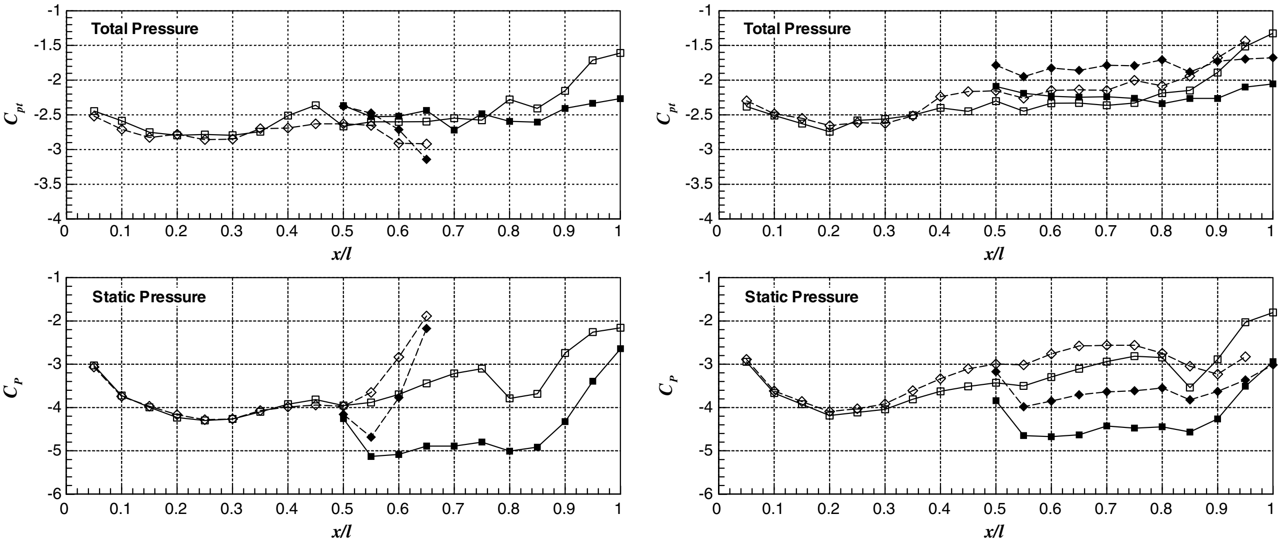

a) Windward vortex system

b) Leeward vortex system

Fig. 19 DDES predictions of total pressure and static pressure coefficient through the vortex cores of case 2 simulations at $\beta = 1\,\mathrm{deg}$ and 2.00 deg for $\alpha = 30.0\,\mathrm{deg}$, $M_\infty = 0.4$, and $Re_{\bar{c}} = 2.68 \times 10^6$. Squares represent $\beta = 1\,\mathrm{deg}$, diamonds represent $\beta = 2\,\mathrm{deg}$, unfilled symbols represent the chine vortex, and filled symbols represent the wing vortex.

D. Comparison of Vortex Properties Before and After Asymmetric Breakdown

To investigate the cause of the sudden asymmetric vortex breakdown, vortex properties before and after breakdown may be compared. In this section, a comparison of vortex properties between case 2 simulations at $\beta = 1$ and 2 deg is completed, including the trajectory, total pressure, and static pressure of the vortex cores.

Plotted in Fig. 18 is a comparison of vortex trajectories between $\beta = 1$ and 2 deg, where squares identify the $\beta = 1$ deg trajectories and diamonds identify the $\beta = 2$ deg trajectories. These trajectories were determined by locating the maximum total pressure depreciation for each vortex. Note from the figure that the trajectories of the windward vortex systems are nearly identical in the y-axis direction. The chine vortex is slightly inboard at $\beta = 2$ deg from $x/l = 0.55$ to breakdown, but it is unlikely that this small difference is the cause of the vortex breakdown. In the z-axis direction, note that at $\beta = 2$ deg, the windward chine vortex is pulled downward and the leading-edge vortex is pulled upward from $x/l = 0.55$ to breakdown; however, this difference is still relatively small and it is unclear if this increased vortex interaction is sufficient to induce breakdown. For the leeward vortex system at $\beta = 2$ deg, the vortices are more outboard and upward from the wing surface, which would account for the aforementioned decrease in suction on the leeward wing with increasing sideslip.

Finally, a comparison of the total pressure C_{pt} and static pressure C_p through the vortex cores is given in Fig. 19. Again, the squares represent $\beta = 1$ deg results and diamonds represent $\beta = 2$ deg results. In addition, unfilled symbols represent the chine vortex and filled symbols represent the leading-edge vortex. We will first concentrate on the total pressure distributions, which can be used as indicator of vortex strength, for which increases in total pressure depreciation indicate a stronger vortex. Both the leeward chine and leading-edge vortices decrease in strength with increasing sideslip. On the windward side, the vortices at $\beta = 1$ and 2 deg are nearly identical in strength up to $x/l = 0.55$. However, for $\beta = 2$ deg, there is a significant increase in both the chine and leading-edge vortices' strength from $x/l = 0.55$ to breakdown. These findings are in agreement with the conclusions of LeMay and Rogers [4] and Grismer and Nelson [5]. Concentrating now on the static pressure distributions, both the windward chine and leading-edge vortices experience a significant adverse pressure gradient before breakdown that is not experienced by any of the other vortices. It is expected that this adverse pressure gradient combined with the increased vortex strength induces breakdown.

IV. Conclusions

Time-accurate delayed detached-eddy simulations were performed on the modular transonic vortex interaction (MTVI) configuration at a Reynolds number of 2.68×10^6 and Mach number of 0.4, for angles of attack up to 30 deg and sideslip up to 5 deg. At zero sideslip, lift and drag predictions are in excellent agreement with the experiment for the full range of angle of attack investigated. At a 30 deg angle of attack, rolling-moment predictions are in excellent agreement with the experiment for sideslip up to 5 deg, accurately predicting the severely nonlinear aerodynamic behavior experienced by the MTVI geometry at approximately 1 deg of sideslip. Such predictive capabilities will improve the design of future fighters and could drastically reduce the cost associated with flight testing new or modified aircraft.

Critical flow features were investigated at a level of detail that is difficult to obtain from experiment. The investigation confirmed that the nonlinear aerodynamic behavior is primarily due to abrupt asymmetric vortex breakdown over the windward wing. The vortex breakdown began at the wing's trailing edge and moved rapidly forward. This resulted in severely asymmetric surface pressure distributions that induce significant positive sectional rolling moments along the wing.

A comparison of vortex properties at 1 and 2 deg sideslip showed only minor changes in vortex trajectory, indicating that this is not the likely cause of the abrupt vortex breakdown. However, at 2 deg sideslip, the windward vortex system experienced a significant increase in total pressure depreciation and an adverse pressure gradient that were not experienced by the leeward vortex system or by the windward vortex system at 1 deg sideslip. This increase in vortex strength combined with the adverse pressure gradient would tend to induce vortex breakdown, but their root cause is still being investigated.

The results of this study will be used to develop and validate lower-order stability and control models being developed for full aircraft configurations at the U.S. Air Force Academy Modeling and Simulation Research Center and the U.S. Air Force Seek Eagle Office.

Acknowledgments

The authors would like to thank the U.S. Air Force Office of Scientific Research and Keith Bergeron of the U.S. Air Force Academy Modeling and Simulation Research Center for their generous financial support, as well as Scott Morton of the U.S. Air Force Seek Eagle Office and the U.S. Department of Defense high-performance computing for their access to the Arctic Region Supercomputing Center. The authors would also like to thank Robert M. Hall of the NASA Langley Research Center for providing the geometry and wind-tunnel data.

References

[1] Erickson, G. E., and Brandon, J. M., "Low-Speed Experimental Study of the Vortex Flow Effects of a Fighter Forebody Having Unconventional Cross-Section," 12th Atmospheric Flight Mechanics Conference, AIAA Paper 85-1798, Aug. 1985.

[2] Rao, D. M., and Bhat, M. K., "A Low-Speed Wind Tunnel Study of Vortex Interaction Control Techniques on a Chine-Forebody/Delta-Wing Configuration," NASA CR-189616, Mar. 1992.

[3] Rom, J., *High Angle of Attack Aerodynamics—Subsonic, Transonic, and Supersonic Flows*, Springer–Verlag, New York, 1992.

[4] LeMay, S., and Rogers, L., "Pneumatic Vortex Flow Control on a 55-Degree Cropped Delta Wing with Chined Forebody," AIAA 16th Aerodynamic Ground Testing Conference, AIAA Paper 90-1430, June 1990.

[5] Grismer, D., and Nelson, R., "The Aerodynamic Effects of Sideslip on Double Delta Wings," 31st Aerospace Sciences Meeting and Exhibit, AIAA Paper 93-0053, Jan. 1993.

[6] Rao, D. M., and Bhat, M. K., "Subsonic Investigations of Vortex Interaction Control For Enhanced High-Alpha Aerodynamics of a Chine Forebody/Delta Wing Configuration," NASA CR-189641, June 1992.

[7] Rao, D. M., and Bhat, M. K., "High-Alpha Vortex Decoupling Investigations on a Chine Forebody/Delta Wing Configuration at Transonic Mach Numbers," NASA CR-189642, June 1992.

[8] Hall, R. M., "Impact of Fuselage Cross Section on the Stability of a Generic Fighter," 16th Applied Aerodynamics Conference, AIAA Paper 98-2725, 1998.

[9] Cummings, R. M., Schiff, L. B., and Duino, J. D., "Experimental Investigation of Tangential Slot Blowing on a Generic Chined Forebody," *Journal of Aircraft*, Vol. 32, No. 4, 1995, pp. 818–824. doi:10.2514/3.46796

[10] Ravi, R., and Mason, W. H., "A Computational Examination of Directional Stability for Smooth and Chined Forebodies at High-α," NASA CR-4465, 1992.

[11] Ravi, R., and Mason, W. H., "Chine-Shaped Forebody Effects on Directional Stability at High-α," *Journal of Aircraft*, Vol. 31, No. 3, 1994, pp. 480–487. doi:10.2514/3.46519

[12] Agosta-Greenman, R. M., Gee, K., Cummings, R. M., and Schiff, L. B., "Computational Investigation of Tangential Slot Blowing Generic Chined Forebody," *Journal of Aircraft*, Vol. 32, No. 4, 1995, pp. 811–817. doi:10.2514/3.46795

[13] Ghaffari, F., "On the Vortical-Flow Prediction Capability of an Unstructured-Grid Euler Solver," 32nd Aerospace Sciences Meeting and Exhibit, AIAA Paper 94-0163, Jan. 1994.

[14] Kinard, T. A., Harris, B. W., and Raj, P., "Computational Simulation of Benign and Burst Vortex Flows," 13th AIAA Applied Aerodynamics Conference, AIAA Paper 95-1815-CP, June 1995.

[15] Finley, D. B., and Karman, S. L., Jr., “Application of Splitflow Unstructured CFD Code to Euler Predictions of a Generic Fighter Model,” 13th AIAA Applied Aerodynamics Conference, AIAA Paper 95-1821-CP, June 1995.

[16] Finley, D. B., “Euler Technology Assessment Program for Preliminary Aircraft Design Employing SPLITFLOW Code with Cartesian Unstructured Grid Method,” NASA CR-4649, Mar. 1995.

[17] Kinard, T. A., Harris, B. W., and Raj, P., “An Assessment of Viscous Effects in Computational Simulation of Benign and Burst Vortex Flows on Generic Fighter Wind-Tunnel Models Using TEAM Code,” NASA CR-4650, Mar. 1995.

[18] Treiber, D. A., and Muilenburg, D. A., “Euler Technology Assessment for Preliminary Aircraft Design Employing OVERFLOW Code with Multiblock Structured-Grid Method,” NASA CR-4651, Mar. 1995.

[19] Kinard, T. A., and Raj, P., “Euler Technology Assessment for Preliminary Aircraft Design—Compressibility Predictions by Employing the Unstructured Grid USM3D Code,” NASA CR-4711, Mar. 1996.

[20] Pirzadeh, S. Z., “A Solution-Adaptive Unstructured Grid Method by Grid Subdivision and Local Remeshing,” *Journal of Aircraft*, Vol. 37, No. 5, 2000, pp. 818–824.
doi:10.2514/2.2675

[21] Raj, P., Finley, D. B., and Ghaffari, F., “An Assessment of CFD Effectiveness for Vortex-Flow Simulation to Meet Preliminary Design Needs Part A—Vortex Flows and High Angle of Attack,” NATO/RTO/AVT Panel Paper No. 47, May 2001.

[22] Spalart, P. R., Deck, S., Shur, M. L., Squires, K. D., Strelets, M. Kh., and Travin, A., “A New Version of Detached-Eddy Simulation, Resistant to Ambiguous Grid Densities,” *Theoretical and Computational Fluid Dynamics*, Vol. 20, No. 3, 2006, pp. 181–195.
doi:10.1007/s00162-006-0015-0

[23] Strang, W. Z., Tomaro, R. F., and Grismer, M. J., “The Defining Methods of Cobalt60: A Parallel, Implicit, Unstructured Euler/Navier Stokes Flow Solver,” 37th AIAA Aerospace Sciences Meeting and Exhibit, AIAA Paper 99-0786, Jan. 1999.

[24] Gottlieb, J. J., and Groth, C. P. T., “Assessment of Riemann Solvers for Unsteady One-Dimensional Inviscid Flows of Perfect Gasses,” *Journal of Computational Physics*, Vol. 78, No. 2, 1988, pp. 437–458.
doi:10.1016/0021-9991(88)90059-9

[25] Tomaro, R. F., Strang, W. Z., and Sankar, L. N., “An Implicit Algorithm for Solving Time Dependent Flows On Unstructured Grids,” 35th AIAA Aerospace Sciences Meeting and Exhibit, AIAA Paper 97-0333, Jan. 1999.

[26] Forsythe, J. R., Squires, K. D., Wurtzler, K. E., and Spalart, P. R., “Detached Eddy Simulation of Fighter Aircraft at High Alpha,” 40th AIAA Aerospace Sciences Meeting and Exhibit, AIAA Paper 2002-0591, Jan. 2002.

[27] Morton, S. A., Steenman, M. B., Cummings, R. M., and Forsythe, J. R., “DES Grid Resolution Issues for Vortical Flows on a Delta Wing and an F18C,” 41st AIAA Aerospace Sciences Meeting and Exhibit, AIAA Paper 2003-1103, Jan. 2003.

[28] Mitchell, A. M., Morton, S. A., Forsythe, J. R., and Cummings, R. M., “Analysis of Delta-Wing Vortical Substructures Using Detached-Eddy Simulation,” *AIAA Journal*, Vol. 44, No. 5, 2006, pp. 964–972.
doi:10.2514/1.755

[29] Spalart, P. R., Jou, W. H., Strelets, M., and Allmaras S. R., “Comments on the Feasibility of LES for Wings, and on a Hybrid RANS/LES approach,” *Advances in DNS/LES, 1st AFOSR International Conference on DNS/LES*, Greyden Press, Columbus. OH, 1997, pp. 137–147.

[30] Spalart, P. R., and Allmaras S. R., “One-Equation Turbulence Model for Aerodynamic Flows,” *La Recherche Aerospatiale: Bulletin Bimestriel de l’Office National d’Etudes et de Recherches Aerospatiales*, Vol. 1, 1994, pp. 5–21.

[31] Menter, F. R., and Kuntz, M., “Adaptation of Eddy-Viscosity Turbulence Models to Unsteady Separated Flow Behind Vehicles,” *Aerodynamics of Heavy Vehicles: Trucks, Busses and Trains*, edited by R. McCallen, F. Browand, and J. Ross, Springer, Berlin, 2004.

[32] Shur, M. L., Strelets, M. K., Travin, A. K., and Spalart, P. R., “Turbulence Modeling in Rotating and Curved Channels: Assessing the Spalart-Shur Correction,” *AIAA Journal*, Vol. 38, No. 5, 2000, pp. 784–792.
doi:10.2514/2.1058

[33] Solidmesh 3D, Software Package, Ver. 5.45, Mississippi State Univ., Computational Simulation and Design Center, Mississippi State, MS, July 2008.

[34] Cummings, R. M., Morton, S. A., and McDaniel, D. R., “Experiences in Accurately Predicting Time-Dependent Flows,” *Progress in Aerospace Sciences*, Vol. 44, No. 4, 2008, pp. 241–257.
doi:10.1016/j.paerosci.2008.01.001

[35] Dubief, Y., and Delcayre, F., “On Coherent-Vortex Identification in Turbulence,” *Journal of Turbulence*, Vol. 1, No. 11, 2000, pp. 1–22.
doi:10.1088/1468-5248/1/1/011

[36] Grismer, D. S., and Nelson, R. C., “Double-Delta-Wing Aerodynamics for Pitching Motions with and Without Sideslip,” *Journal of Aircraft*, Vol. 32, No. 6, 1995, pp. 1303–1311.
doi:10.2514/3.46879